Vertically Oriented Arrays of ReS$_2$ Nanosheets for Electrochemical Energy Storage and Electrocatalysis

Jian Gao,[†,∇] Lu Li,[‡,∇] Jiawei Tan,[†] Hao Sun,[‖] Baichang Li,[†] Juan Carlos Idrobo,[⊥] Chandra Veer Singh,[#] Toh-Ming Lu,[§] and Nikhil Koratkar*[,†,‡]

[†]Materials Science and Engineering, [‡]Mechanical, Aerospace and Nuclear Engineering, and [§]Physics, Applied Physics, and Astronomy, Rensselaer Polytechnic Institute, Troy, New York 12180, United States

[‖]Department of Mechanical and Industrial Engineering, University of Toronto, Toronto, Ontario M5S 3G8, Canada

[⊥]Center for Nanophase Materials Sciences, Oak Ridge National Laboratory, Oak Ridge, Tennessee 37831, United States

[#]Department of Materials Science and Engineering, University of Toronto, Toronto, Ontario M5S 3E4, Canada

S Supporting Information

ABSTRACT: Transition-metal dichalcogenide (TMD) nanolayers show potential as high-performance catalysts in energy conversion and storage devices. Synthetic TMDs produced by chemical-vapor deposition (CVD) methods tend to grow parallel to the growth substrate. Here, we show that with the right precursors and appropriate tuning of the CVD growth conditions, ReS$_2$ nanosheets can be made to orient perpendicular to the growth substrate. This accomplishes two important objectives; first, it drastically increases the wetted or exposed surface area of the ReS$_2$ sheets, and second, it exposes the sharp edges and corners of the ReS$_2$ sheets. We show that these structural features of the vertically grown ReS$_2$ sheets can be exploited to significantly improve their performance as polysulfide immobilizers and electrochemical catalysts in lithium–sulfur (Li–S) batteries and in hydrogen evolution reactions (HER). After 300 cycles, the specific capacity of the Li–S battery with vertical ReS$_2$ catalyst is retained above 750 mA h g^{-1}, with only ~0.063% capacity decay per cycle, much better than the baseline battery (without ReS$_2$), which shows ~0.184% capacity decay per cycle under the same test conditions. As a HER catalyst, the vertical ReS$_2$ provides very small onset overpotential (<100 mV) and an exceptional exchange-current density (~67.6 μA/cm^2), which is vastly superior to the baseline electrode without ReS$_2$.

KEYWORDS: Transition metal dichalcogenides, ReS$_2$ nanosheets, chemical vapor deposition, lithium–sulfur batteries, hydrogen evolution reaction
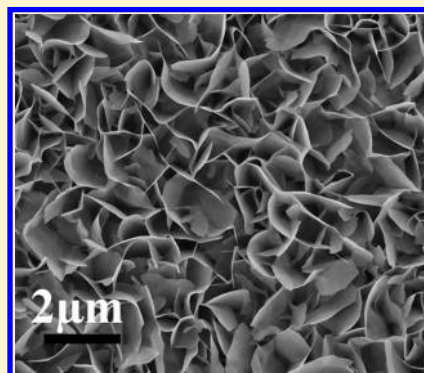
R ecent years have seen renewed interest in van der Waals solids such as transition metal dichalcogenides (TMDs).[1−5] These materials are composed of atomic layers of chalcogens (X = S or Se) and group VI transition metals (M = Mo, W, or Re) arranged in a trigonal prismatic (MX$_2$) structure.[6,7] Atomically thin monolayers of this material can be mechanically exfoliated from the bulk (e.g., by using the Scotch-tape method) but can also be synthetically produced by chemical vapor deposition (CVD) methods. Briefly, in CVD-based approaches, the growth substrate (e.g., Si−SiO$_2$ wafer) is placed above a powdered transition-metal precursor (e.g., MO$_3$) inside a quartz tube under argon flow. The chalcogen (X) is placed upstream in a cooler region of the tube. When the temperature in the central portion of the furnace is raised to the target temperature, both the MO$_3$ and X are cosublimated, and MX$_2$ growth begins on the substrate. This approach has been used in the literature[8−19] to produce a variety of monolayer TMD materials including MoS$_2$, WS$_2$, ReS$_2$, MoSe$_2$, and WSe$_2$. Figure S1 shows typical monolayer WS$_2$ films grown by this approach in our lab (the TMD growth is always parallel to the growth substrate).

Although there are some reports of flowerlike MoS$_2$ films,[3,20] the vast majority of TMD films produced by CVD approaches grow parallel to the substrate and lie flat on the substrate.[8−19] Here, we report that although MoS$_2$ and WS$_2$ films tend to grow parallel to the substrate, under similar CVD growth conditions, ReS$_2$ nanosheets show a remarkable tendency to bend and stand vertically on the growth substrate. In fact, the propensity for ReS$_2$ to orient itself perpendicular to the growth substrate is independent of the substrate material used or the packing density (i.e., intersheet separation) of the ReS$_2$ sheets on the substrate. Such TMD films that are oriented perpendicular to the growth substrate provide two key attributes that differ from traditional planar TMD films: (1) for a planar TMD film, there is no net increase in the wetted surface area. In contrast, for the perpendicular TMD film and for TMD sheets of ~10 × 10 μm dimensions with a packing density of ~10^8 cm^{-2}, the ratio of the surface area of such a
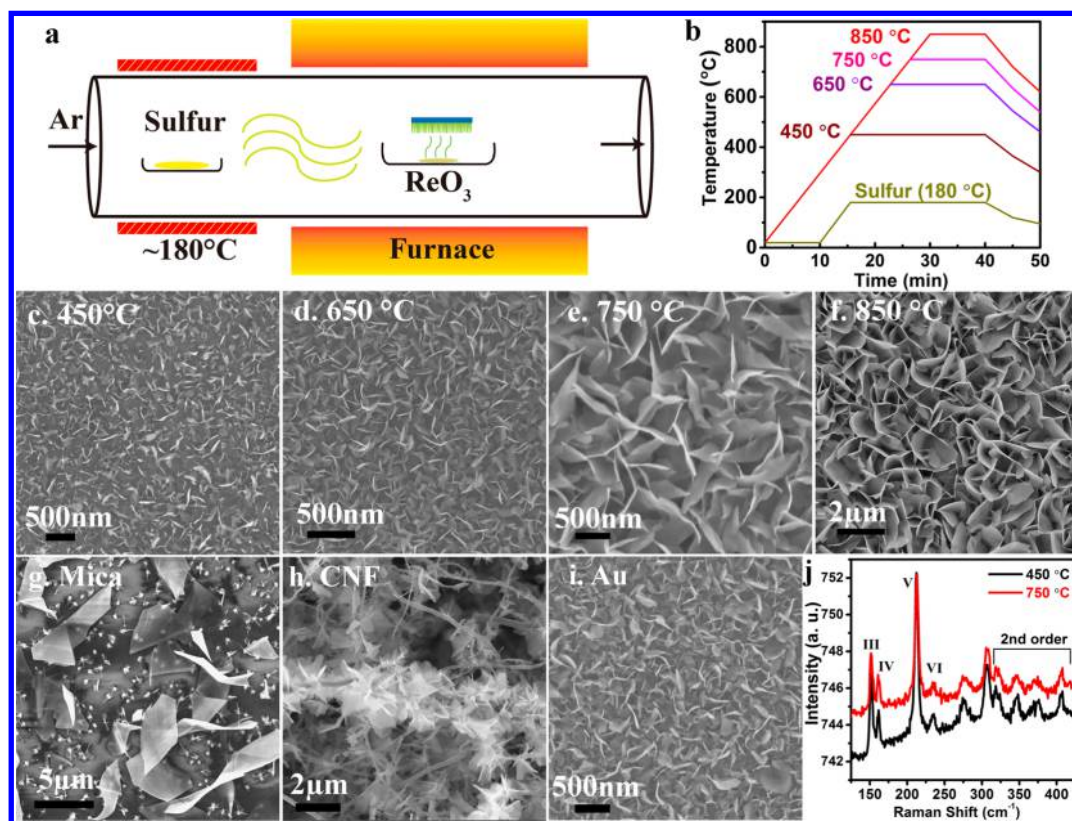
Figure 1. Vertical ReS$_2$ growth and morphology. (a) Schematic of ReS$_2$ growth. (b) Growth-temperature profile. (c−f) SEM images of ReS$_2$ grown on SiO$_2$−Si at (c) ∼450 °C, (d) ∼650 °C, (e) ∼750 °C, and (f) ∼850 °C. The sulfur was provided once the furnace temperature reached ∼450 °C, as indicated in panel b. Vertical ReS$_2$ could be successfully grown on a variety of substrates, including (g) mica (synthesized at the same growth conditions as the sample in Figure S3a), (h) carbon nanofibers (CNF), and (i) gold (Au) foil. Although the packing density, flake size, etc. can be affected by the substrate, the vertical growth character appears to be substrate-independent. (j) Raman spectra of the ReS$_2$ film from panels c and e.

textured surface to its projected flat surface area is ∼100. This surface area increase can be controlled by varying the dimensions and packing density of the TMD sheets. It should be noted that the above projections for surface area increase assume full coverage of the planar TMD film. For situations involving partial coverage or gaps between the 2D layers, the surface area of planar TMD films can also be significantly increased, and (2) the atomically sharp edges and sharp corners of the TMD sheets are fully exposed when the sheets are lifted off and oriented perpendicular to the growth substrate. The large curvature of the sheet edges and sharp corners will generate high local electric fields in these regions; this, along with the fact that the catalytically active transition metal atoms are exposed along the sheet edges, has obvious implications for electrochemical catalysis or field emission from such surfaces.

In this work, we demonstrate that one can select CVD process parameters to make it energetically favorable for ReS$_2$ nanosheets to orient themselves perpendicular to the growth substrate. Moreover, this vertical orientation of the ReS$_2$ nanosheets is substrate-independent and is observed on SiO$_2$−Si, mica, and carbon as well as gold. We also demonstrate how the packing density, sheet size, and crystal quality of the ReS$_2$ sheets can be controlled by adjusting the CVD growth conditions. We show that the enhanced surface area and sharp exposed edges of such vertically oriented ReS$_2$ films have important implications for energy-storage devices such as lithium−sulfur (Li−S) batteries. We further demonstrate that the increased amount of edges and surfaces greatly enhances the catalytic activity of such films for production of hydrogen,

which is an important fuel for combustion and fuel-cell applications. Our results suggest that perpendicular TMD−substrate interfaces represent a new class of catalyst−electrode structures that could offer significant benefits in electrochemical energy storage and catalysis applications.

Typical 2D semiconducting TMDs such as MoS$_2$ and WS$_2$ exhibit a direct band gap only in the monolayer limit. However, ReS$_2$ is different from other 2D semiconducting TMDs and exhibits a direct band gap[19] for both bulk and monolayer samples, presumably due to weak interlayer coupling. Recently, it has been shown that CVD methods can be used to grow ReS$_2$ sheets parallel to the surfaces of SiO$_2$−Si substrates. For example, hexagonal-shape ReS$_2$ has been synthesized using ammonium perrhenate (NH$_4$ReO$_4$)[21] and Re metal,[22] and near-triangular ReS$_2$ has been achieved by using ReO$_3$ as the precursor.[23] ReS$_2$ deposition on a graphene foam has also been demonstrated by a two-step method: dip-coating (NH$_4$ReO$_4$) on graphene foam followed by annealing in H$_2$S environment.[24] In this study, we present a method of growing vertical flowerlike ReS$_2$ sheets by appropriate control of the CVD process parameters. Briefly, an alumina boat with ∼1 mg of ReO$_3$ powder and the growth substrate was loaded into the center of a ∼1 in. furnace tube, and another boat with ∼500 mg of sulfur pellets was loaded upstream wrapped with a heating tape (Figure 1a). The growth temperature profiles are illustrated in Figure 1b. As shown in Figure 1c−f, we are able to grow vertical ReS$_2$ sheets on SiO$_2$−Si substrates from 450 to 850 °C. At lower growth temperature of 450 °C, we obtain relatively small vertical ReS$_2$ flakes with a size of ∼200 nm
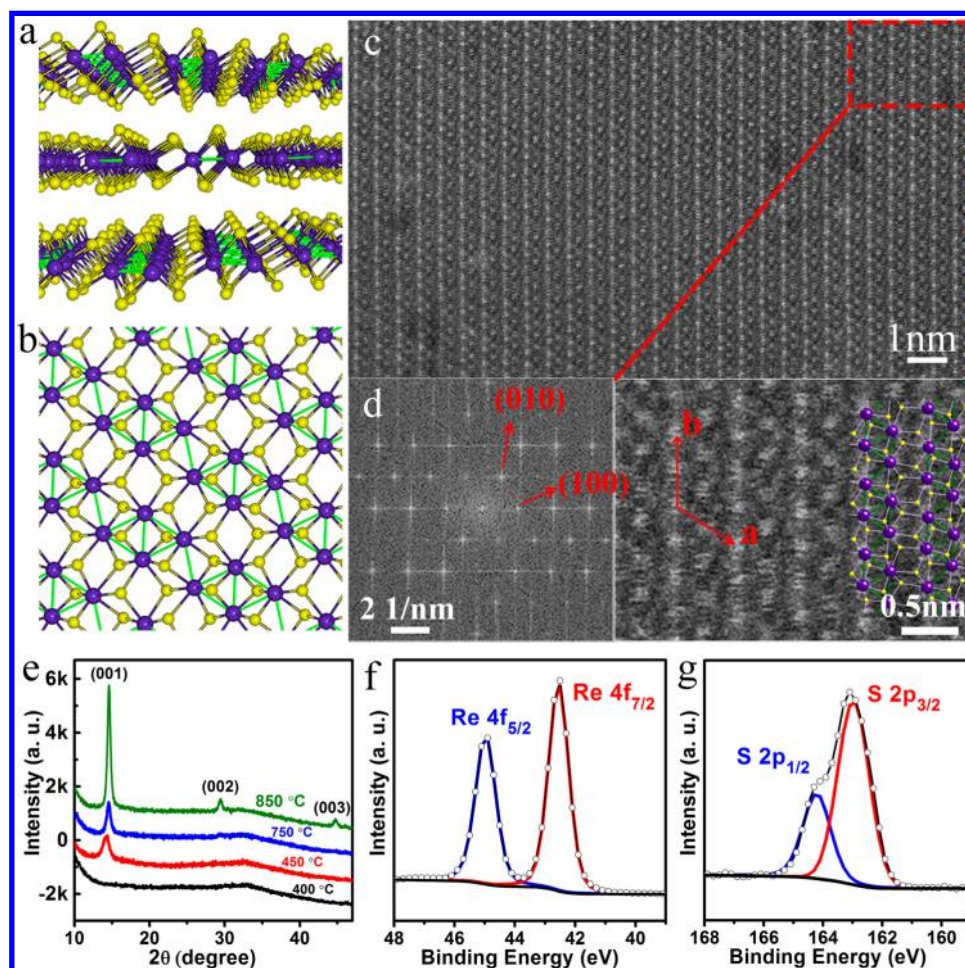
Figure 2. Structural and chemical characterizations. (a,b) Structural schematics of the distorted 1T ReS_2 structure. (c) Z-contrast STEM image of ReS_2 sheet grown at ~750 °C. (d) FFT of the STEM image. (e) XRD patterns of ReS_2 grown at different temperatures (sulfur was introduced once the furnace temperature reached ~450 °C for all cases except for ReS_2 growth at ~400 °C, for which the sulfur introduction temperature coincided with the growth temperature). XPS spectra showing Re 4f (f) and S 2p (g) core level peaks with Gaussian−Lorentz fitting. The ~284.8 eV adventitious C 1s peak was used for charging corrections.

(Figure S2). With increasing the growth temperature, the flake size are increased to several microns due to faster growth rate at raised temperature. Furthermore, we find that the sulfur introduction time plays a crucial role in controlling the spatial density of vertical sheets. To ensure that we obtain a high spatial density of vertical sheets, we have to introduce the sulfur (see Figure 1b) before the furnace temperature reaches ~450 °C. This is because above ~400 °C, ReO_3 begins to decompose to Re_2O_7 (which sublimes easily) and ReO_2 (which is less volatile). As a consequence, at ~450 °C, there is still abundant Re precursor available for reaction with S to form ReS_2. However, if the sulfur is introduced when the furnace temperature is much higher than 450 °C (for example, at ~750 or ~1000 °C), a substantial portion of the ReO_3 precursor is already decomposed to nonvolatile ReO_2 during the temperature ramping. This significantly reduces the Re precursor concentration, which favors fewer nucleation sites but with a faster growth rate, leading to large sheet sizes. Typical samples produced with sulfur introduction into the surface at ~750 °C are shown in Figure S3a, showing reduced spatial density of ReS_2 sheets with large sheet size. At a temperature of ~1000 °C (Figure S3b), the spatial density of the ReS_2 flakes is by far the lowest, which further demonstrates that the sulfur introduction time is critical in growing high-density, ReS_2

sheets. To confirm the above hypothesis, we annealed the ReO_3 powder at ~550 °C for ~30 min under Ar environment and discovered that almost all of the ReO_3 precursor was converted to nonvolatile ReO_2, and no rhenium compounds were deposited on the SiO_2 substrate (Figure S4), which explains the low spatial density of ReS_2 sheets when the sulfur is introduced at high temperatures.

In addition to the temperature and sulfur control, we have also successfully grown vertical ReS_2 on different substrates (Figure 1g−i), including mica, carbon nanofibers, and gold foils, on all of which we see the same universal vertical-growth character. The vertical orientation of ReS_2 is also independent of the intersheet spacing and is observed for densely packed (Figure 1c−f) as well as sparsely packed (Figure 1g, Figure S3) films. Because the vertical growth mode is substrate- and packing-density-independent, this effect could presumably be related to stress build-up in the ReS_2 sheets, which can cause the sheets to curve up and lift off the surface. The origin for such a stress build-up is not clear at this point and will require further investigation. Another contributory factor to the vertical growth mode could be the rapid supply of Re (from fast evaporation of ReO_3 or Re_2O_7) that could serve to suppress the atomic migration of Re and S precursors on the surface of the growth substrate. Similarly, it is likely that a weak ReS_2
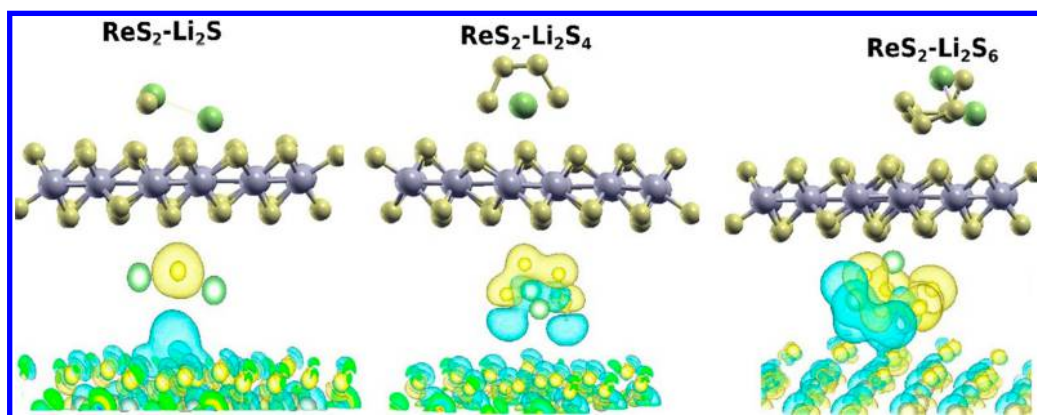
Figure 3. DFT simulation of polysulfide–ReS$_2$ interactions. Optimized atomic positions and charge-density plots with isosurface level of 0.028, 0.033, and 0.025 e/Bohr^3 for ReS$_2$–Li$_2$S, ReS$_2$–Li$_2$S$_4$, and ReS$_2$–Li$_2$S$_6$ systems, respectively. Here, the yellow and green balls symbolize sulfur and lithium atoms, respectively. Rhenium atoms are blue in the positions plot and gray in the charge-density plot.

substrate interaction also contributes to the vertical growth mode. In-depth modeling and simulation work will be needed to further elucidate these mechanisms and pinpoint the underlying causes for the substrate-independent perpendicular orientation of the ReS$_2$ sheets in our as-grown films.

We characterized the as-prepared ReS$_2$ films by room-temperature Raman spectroscopy with 532 nm laser. The samples grown at different temperatures exhibit similar Raman spectra, which are illustrated in Figure 1j; the A$_g$ vibrational modes are labeled in the plot by Roman numerals. The Raman shift of III, IV, V, and VI peaks are located at 151.5, 161.7, 212.4, and 234.8 cm^{-1}, respectively, which are consistent with few-layer ReS$_2$ Raman spectra.[25,26] To analyze the crystal structure and orientation of the as-prepared ReS$_2$, we have performed aberration-corrected scanning transmission electron microscopy (STEM) by transferring the ReS$_2$ grown at ~750 °C onto a TEM grid. Figure 2c shows a Z-contrast image of the as-prepared ReS$_2$ flake along the 001 crystallographic orientation. The zoomed STEM image is well-overlapped with the schematic ReS$_2$ structure, as shown in the inset of Figure 2c. It should be noted that because each Re atom has seven valence electrons, the extra electron contributes to the formation of Re–Re bonds (as indicated by the green lines in Figure 2a,b), which distorts the 1T structure.[19] The corresponding FFT image (Figure 2d) also indicates that the ReS$_2$ flake is hexagonal and [001] oriented, with the (100) and (010) planes labeled.

To analyze the crystal structure of the samples grown at different temperatures, we performed X-ray diffraction (XRD) $\theta/2\theta$ scans on the samples. As shown in Figure 2e (for ReS$_2$ grown at ~850 °C), peaks at 14.58, 29.45, and 44.78° are present, which can be indexed to triclinic ReS$_2$ (ICDD, reference number, 00-052-0818), belonging to the P-1 symmetry group. The first peak at ~14.58° is attributed to the (001) peak, and the lattice constant c is calculated as ~6.08 Å. As the ReS$_2$ growth temperature was decreased from ~850 °C to ~450 °C, the (001) 2θ peak gradually decreased to ~14.3°, and the (001) plane distance increased to ~6.19 Å. We also find that the sulfur introduction time plays an important role in forming high-crystal-quality ReS$_2$. For example, if we provide sulfur at low temperatures (~400 °C), then reaction with sulfur induces films that are relatively more amorphous and oxygen-rich (S depleted), which is confirmed by the energy-dispersive X-ray spectroscopy (EDS) analysis in Figure S2. When the sulfur is introduced at higher temperatures, the

crystal quality and size of the ReS$_2$ sheets is significantly improved at the expense of lower packing density of the vertical ReS$_2$ sheets. Finally, we have utilized X-ray photoelectron spectroscopy (XPS) to study the chemical states of the synthesized samples. As shown in Figure 2f,g, the Re 4f$_{7/2}$ and Re 4f$_{5/2}$ core-level peaks are located at ~42.8 and ~45.2 eV, and S 2p$_{3/2}$ and S 2p$_{1/2}$ peaks are at ~163.2 and ~164.3 eV, which is expected for ReS$_2$.[27] We also calculated the Re-to-S ratio from XPS (see the Supporting Information), which was ~1:1.92 (for samples synthesized at ~750 °C), which is slightly substoichiometric, indicating sulfur vacancies in the ReS$_2$ flakes. The S depletion increases at lower growth temperatures; for example, samples synthesized at ~500 °C showed a Re-to-S ratio of ~1:1.74.

The perpendicular ReS$_2$–substrate architectures synthesized in Figure 1 have two key attributes that distinguish them from conventional planar TMD films, the first being the increase in the wetted surface area obtained by lifting the individual sheet off the substrate platform, and the second being that the sharp sheet edges, corners, and tips are now fully exposed and can be exploited for applications in electrochemistry and catalysis. An important technological application in which the aforementioned attributes of perpendicular ReS$_2$–substrate junctions could be exploited is lithium–sulfur (Li–S) batteries. Due to the advantages of high specific capacity (1675 mAh g^{-1}) and high specific-energy density (2600 Wh kg^{1-}) compared to the other rechargeable battery systems (such as lead–acid batteries, nickel–metal hydride batteries, and lithium ion batteries), Li–S batteries have been regarded as one of the most promising power sources for portable electronics, power tools, and electric vehicles.[28,29] However, the dissolution of lithium polysulfides during the charge and discharge processes leads to poor cycling stability.[30,31] Besides, the solid–liquid reaction mechanism of Li–S batteries is kinetically sluggish, owing to the insulating nature of sulfur and its discharge products.[31,32] To investigate whether ReS$_2$ surfaces can trap lithium polysulfides, we performed density functional theory (DFT) calculations (see the Supporting Information) to examine how the binding strength of the Li–S end of linear lithium polysulfides is influenced by ReS$_2$. The binding energies for Li$_2$S, Li$_2$S$_4$, and Li$_2$S$_6$ systems over two-dimensional ReS$_2$ surface are calculated as 2.66, 2.24, and 2.43 eV, respectively. Notably, the binding energies for all Li$_x$S$_y$ structures to ReS$_2$ are observed to be much higher than to a carbon hexatomic ring network (~0.5–1 eV).[33] This suggests that ReS$_2$ surfaces can be far more effective
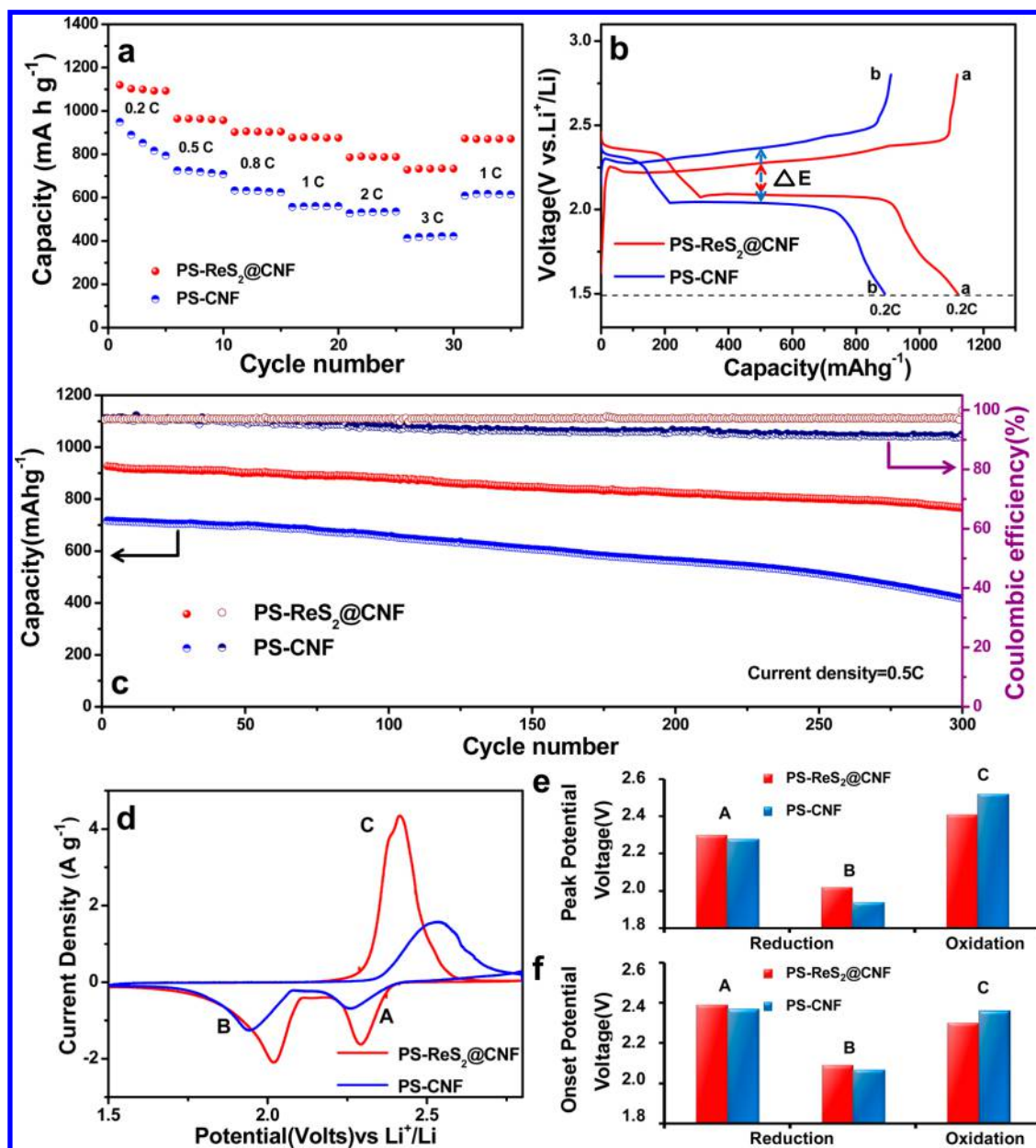
Figure 4. Electrochemical performance comparison of Li−S batteries with PS−ReS$_2$@CNF and PS−CNF electrodes. (a) Specific capacity at different current densities (1 C = 1675 mA g^{-1}). (b) Galvanostatic charge−discharge profiles of the second cycle at ∼0.2 C within a potential window of 1.5−2.8 V vs Li$^+$ and Li^0. (c) Cycling stability and Coulombic efficiency of the PS−ReS$_2$@CNF and baseline PS−CNF. (d) CV profiles of the PS−ReS$_2$@CNF and baseline PS−CNF electrodes. (e,f) Corresponding peak potentials and onset potentials of PS−ReS$_2$@CNF and PS−CNF electrodes in the Li−S battery.

at adsorbing and trapping polysulfides than conventional carbon-based surfaces. This enhancement is mostly attributed to the strong ionic attractions between negatively charged S atoms of ReS$_2$ and positively charged Li cations of Li$_x$S$_y$ molecules. This absorption is evident in Figure 3, where we have plotted the relaxed atomic positions of different molecules and charge-density redistribution on the surface of ReS$_2$. Structural analysis reveals that during adsorption, Li−S bond in Li$_2$S$_6$ gets stretched from ∼2.36 to ∼2.47 Å as the Li atoms are attracted by the S atoms on the surfaces of the ReS$_2$. The relative bond length elongation for Li$_2$S$_4$ and Li$_2$S are observed to be smaller than that for Li$_2$S$_6$. In response to the polysulfide adsorption, the ReS$_2$ sheet also undergoes small structural perturbation and surface-charge-density redistribution (Figure

3). The four Re atoms in the unit cell are displaced closer to each other while the S atoms are displaced out of the plane. The electrons tended to concentrate in the region between the polysulfide molecules and ReS$_2$ surface.

Because the binding energy of polysulfides (2.24−2.66 eV) to ReS$_2$ surfaces are significantly higher than that of carbon (∼0.5−1 eV), our analysis suggests that ReS$_2$ nanosheets decorated on a conductive carbon electrode could help to alleviate the dissolution of lithium polysulfides and achieve a corresponding improvement in the battery performance. In this context, vertical ReS$_2$ sheets are clearly superior to planar ReS$_2$ because the vertical sheets will maximize the wetted or exposed surface area of the electrode for polysulfide immobilization. To investigate this, we constructed a Li−S battery using dissolved
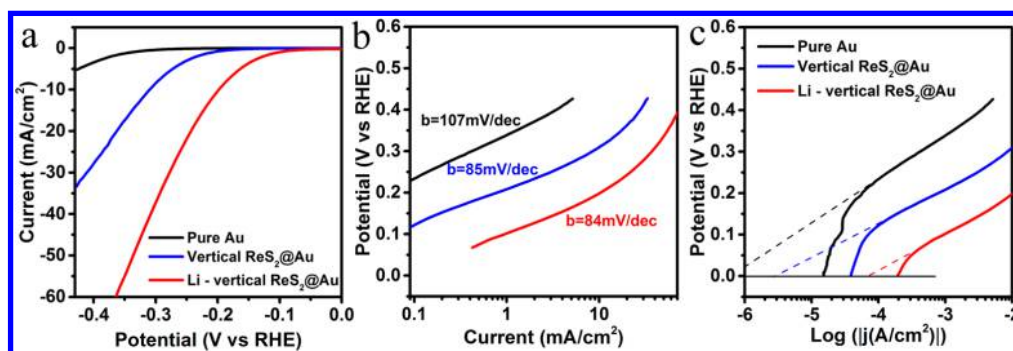
Figure 5. HER performance of different electrodes. (a) Polarization curves obtained with lithiated vertical ReS$_2$@Au, as-prepared vertical ReS$_2$@Au, and pure Au foil. (b) The corresponding Tafel plots. (c) Calculated exchange-current densities by applying the extrapolation method to the Tafel plots.

lithium polysulfide (PS) as the active material. A free-standing carbon nanofiber (CNF) membrane electrode (Figure S5) was used as the substrate, and then PS solution (Li$_2$S$_6$) was added, forming the baseline PS−CNF electrode, which serves as the control. To evaluate the effect of ReS$_2$, we grew vertical ReS$_2$ nanosheets on a CNF membrane at a growth temperature of ∼750 °C; the structure of this composite (ReS$_2$@CNF) is shown in Figure 1h. The same amount of PS (as for the control sample without ReS$_2$) was also added as the active material (PS−ReS$_2$@CNF electrode). Galvanostatic charge−discharge testing of PS−ReS$_2$@CNF and the baseline PS−CNF electrodes are shown in Figure 4a. The discharge capacities for the PS−ReS$_2$@CNF at 0.2C, 0.5C, 0.8C, 1C, 2C, and 3C rates are ∼1100, ∼ 960, ∼903, ∼876, ∼787, and ∼732 mAh g^{-1}, respectively, indicating high capacity and rate capability. Note that the background capacity from ReS$_2$ was relatively small (Figure S6).

In contrast, under the same test conditions, the average discharge capacity of the PS−CNF is significantly lower (Figure 4a), which suggests significant dissolution of polysulfides (in the cathode) into the electrolyte. The galvanostatic charge−discharge behavior of the Li−S battery was evaluated at 0.2 C within a potential window of 1.5−2.8 V versus Li$^+$−Li^0, as shown in Figure 4b. A pair of plateaus are observed in both discharge curves, which corresponds to the reduction of sulfur to long-chain lithium polysulfides at about 2.3−2.4 V and to the formation of short-chain Li$_2$S$_2$−Li$_2$S at around 2.1 V. A relative low polarization of ∼190 mV at 0.2 C was observed between charge and discharge curves in the PS−ReS$_2$@CNF electrode, and the polarization in the PS−CNF electrode is much higher up to ∼310 mV, which suggests an improved electrochemical reaction dynamics in the battery with a PS−ReS$_2$@CNF electrode. Figure 4c shows the long-term cycling performance of PS−ReS$_2$@CNF electrode and PS−CNF electrode at a current density of 0.5C. After 300 cycles, the specific capacity of the PS−ReS$_2$@CNF electrode is retained above 750 mAh g^{-1} with only ∼0.063% capacity decay per cycle, much better than the PS−CNF electrode with a capacity of ∼410 mAh g^{-1} (∼0.184% capacity decay per cycle) under the same test condition. The Coulombic efficiency of the Li−S cell with the baseline PS−CNF electrode is also significantly lower (Figure 4c) in comparison to the PS−ReS$_2$@CNF electrode.

Cyclic voltammetry (CV) testing (Figure 4d) was used to study the reaction kinetics of the battery system. The two reduction peaks for the PS−ReS$_2$@CNF electrode at ∼2.3 V and ∼2.02 V correspond to the two-step conversions of sulfur (S$_8$) to high-order lithium polysulfides (Li$_2$S$_x$, 4 ≤ x ≤ 8) and

high-order lithium polysulfides to Li$_2$S$_2$−Li$_2$S, respectively. In the corresponding backward-oxidation process, one peak is observed at ∼2.41 V, suggesting that lithium sulfides convert to soluble lithium polysulfides and then finally into sulfur.[34] The peak-potential (Figure 4e) results obtained from the CV data indicates increased redox kinetics and smaller polarization for the PS−ReS$_2$@CNF electrode compared to PS−CNF. The onset potentials of PS−ReS$_2$@CNF and PS−CNF electrodes obtained from the CV profiles are shown in Figure 4f. The onset potential is defined as the potential at which ∼10% of the current value at the peak potential is reached.[35] From Figure 4f, we determined that the onset potential of the PS−ReS$_2$@CNF electrode in the oxidation reaction is lower by ∼60 mV compared to PS−CNF. With respect to the reduction reactions, the onset potentials of the PS−ReS$_2$@CNF electrode (∼2.39 and ∼2.09 V) are ∼30 mV higher than the baseline PS−CNF electrode. Considering the increased peak potentials and onset potentials of the cathodic peaks and the decreased peak potentials and onset potentials of anodic peak, it is evident that the presence of ReS$_2$ significantly accelerates the redox processes in the Li−S battery system. The ability of the ReS$_2$ to catalyze the electrochemical reactions of the Li−S battery could be related to local enhancement in the electric field near the sharp edges and corners of the vertical ReS$_2$ sheets. Therefore, the effect of ReS$_2$ is two-fold: (1) the presence of ReS$_2$ increases the redox kinetics and catalyzes the electrochemical reactions in the Li−S battery, and (2) ReS$_2$ has outstanding adsorption ability with polysulfides, which suppresses the dissolution of polysulfides and enhances the cycle stability of the Li−S battery. The enhanced catalytic activity in conjunction with the suppression of polysulfide dissolution into the electrolyte enables significant improvement in the Li−S battery performance.

The perpendicular ReS$_2$−substrate films that we have synthesized can also have important implications for electrochemical hydrogen evolution (HER). Previous studies have explored the use of TMDs (MoS$_2$,[36−39] WS$_2$,[40] and ReS$_2$[27]) as HER catalysts. However, in the prior work, the TMD catalyst films are usually aligned parallel to the substrate. If the TMD sheets can be made to orient perpendicular to the substrate, then more edges and surfaces of the TMD can be exposed. It is well-established that metallic edges of MoS$_2$ are catalytically active sites for HER,[41−43] and although the active sites of ReS$_2$ are yet to be identified, greater exposure to the edges and exposed surfaces (with defects) of the ReS$_2$ in the catalyst film is generally desired. The vertical sheets will also exhibit higher localized electric field intensity near sharp edges and corners,

which is also beneficial for HER. To investigate the catalytic performance, we synthesized vertical ReS_2 on Au foil by CVD at ~750 °C (see Figure 1i). The bare Au foil (as the control) and vertical ReS_2@Au foil were used as working electrodes in three-electrode electrochemical measurements with ~0.5 M H_2SO_4 aqueous electrolyte. As can be seen from Figure 5a, the vertical ReS_2@Au exhibits a small onset overpotential (η) of ~200 mV (compared to ~400 mV for bare Au), beyond which the cathodic current increases rapidly under more negative potentials. In an effort to further improve performance, we carried out lithiation of the vertical ReS_2@Au (using n-butyl lithium treatment; see the Supporting Information) and found that the lithiated sample displayed an even smaller onset overpotential ($\eta < 100$ mV, Figure 5a). To investigate the n-butyl lithium treatment, we checked the morphology of the flakes pre- and post- lithiation (Figure S7). After the treatment, the flakes remain vertical, but some damage to the flakes is noticeable after the treatment, which is shown in the inset of Figure S7. Such damage induced by the treatment is expected to introduce more active (defect) sites. We have also characterized the Raman spectra of the ReS_2 pre- and post-lithium intercalation. As can be seen in Figure S7c, lithium treatment did not change the symmetry of ReS_2 as the Raman peaks positions did not change. Therefore, the enhanced HER is presumably related to increased active sites due to the introduction of defects[44] and strains induced by the lithiation.[44,45] Further in-depth study will be required to study these effects in more detail. Our ReS_2 catalyst films also display high stability in HER. After 1000 cycles of continuous operation at a testing rate of 10 mV/s and a step of 10 mV, we find only ~15% decay in the electrocatalytic current density, as shown in Figure S8. On the basis of our data, we determined that the fitted Tafel slopes are ~103, ~85, and ~84 mV/dec for baseline Au, vertical ReS_2@Au, and lithiated vertical ReS_2@Au (Figure 5b). We have also calculated the exchange current density (J_0) by applying the extrapolation method to the Tafel plots (Figure 5c). The lithiated vertical ReS_2@Au shows a remarkable J_0 of ~67.6 $\mu A/cm^2$, which is significantly higher than previous studies with TMD catalysts,[46] indicating that such lithiated vertical ReS_2 on gold architectures show outstanding potential as electrochemical catalysts for hydrogen evolution reactions.

In summary, the majority of work on TMD materials has so far been limited to planar devices. Although TMD−TMD heterojunctions and heterointerfaces have been extensively studied in recent years, the main focus has remained on planar devices with the TMD sheets oriented parallel to the growth substrate. For the majority of electronics and optoelectronics devices, the focus on planar devices is appropriate. However, for electrochemical catalysis, perpendicular TMD−substrate heterojunctions can offer some unique advantages and benefits over planar devices. We demonstrate two such applications in this work in the context of vertically oriented ReS_2 nanosheets. The first is as a catalyst that accelerates redox processes and limits polysulfide diffusion in Li−S batteries, and the second is a high-performance catalyst for hydrogen evolution with low onset overpotentials and high exchange-current density.

Another important aspect of this work is that we have demonstrated that one can select CVD process parameters to make it energetically favorable for ReS_2 nanosheets to orient themselves perpendicular to the growth substrate. Moreover, this vertical orientation of the ReS_2 nanosheets appears to be independent of the substrate used and is observed on SiO_2−Si, mica, and carbon as well as gold. We also demonstrate how the packing density, sheet size, and crystal quality of the ReS_2 sheets can be controlled by adjusting the CVD growth conditions. Compared to other types of TMDs (such as MoS_2 or WS_2), ReS_2 exhibits a much greater propensity to orient itself vertical to the growth substrate. The underlying reasons for this are not clear at this point and will require further in-depth study. Our hope is that this study will stimulate the attention of the research community toward the development and testing of perpendicular TMD catalyst-electrode structures for various applications in electrochemistry.

■ ASSOCIATED CONTENT

Ⓢ Supporting Information

The Supporting Information is available free of charge on the ACS Publications website at DOI: 10.1021/acs.nanolett.6b01180.

Details of the materials and methods and stoichiometric calculations from XPS. Figures showing the chemical vapor deposition facility used in our laboratory to grow TMD materials; schematic illustration of the co-sublimation method for TMD growth; SEM micrograph of a typical monolayer WS_2 sheet grown in our lab by using this approach; HR-STEM confirmation of WS_2 structure; structure of vertical ReS_2 nanosheets synthesized at growth temperatures and sulfur introduction temperatures of below 450 °C; structure of vertical ReS_2 nanosheets synthesized at growth temperatures and sulfur introduction temperatures of 750 and 1000 °C; control experiment for ReO_3 precursor decomposition without introduction of sulfur into the reactor; photograph and SEM images of the free-standing CNF membrane; background capacity of the ReS_2 material in Li−S battery, characterization of the structure of the lithiated ReS_2 electrode; SEM images and Raman spectra of ReS_2 and lithiated ReS_2; and polarization curve of n-butyl lithium treated vertical ReS_2@Au after continuous operation for 1000 cycles. (PDF)

■ AUTHOR INFORMATION

Corresponding Author

*E-mail: koratn@rpi.edu.

Author Contributions

∇J.G. and L.L. contributed equally in this manuscript.

Notes

The authors declare no competing financial interest.

■ ACKNOWLEDGMENTS

■ REFERENCES

(1) Cheng, R.; Jiang, S.; Chen, Y.; Liu, Y.; Weiss, N.; Cheng, H. C.; Wu, H.; Huang, Y.; Duan, X. F. *Nat. Commun.* **2014**, *5*, 5143.

(2) Chang, H. Y.; Yang, S. X.; Lee, J. H.; Tao, L.; Hwang, W. S.; Jena, D.; Lu, N. S.; Akinwande, D. *ACS Nano* **2013**, *7*, 5446−5452.

(3) Mak, K. F.; Lee, C.; Hone, J.; Shan, J.; Heinz, T. F. *Phys. Rev. Lett.* **2010**, *105*, 136805.

(4) Zhu, B. R.; Chen, X.; Cui, X. D. *Sci. Rep.* **2015**, *5*, 9218.

(5) Chow, P. K.; Jacobs-Gedrim, R. B.; Gao, J.; Lu, T. M.; Yu, B.; Terrones, H.; Koratkar, N. *ACS Nano* **2015**, *9*, 1520−1527.

(6) Li, L. K.; Yu, Y. J.; Ye, G. J.; Ge, Q. Q.; Ou, X. D.; Wu, H.; Feng, D. L.; Chen, X. H.; Zhang, Y. B. *Nat. Nanotechnol.* **2014**, *9*, 372−377.

(7) Favron, A.; Gaufres, E.; Fossard, F.; Phaneuf-L'Heureux, A. L.; Tang, N. Y. W.; Levesque, P. L.; Loiseau, A.; Leonelli, R.; Francoeur, S.; Martel, R. *Nat. Mater.* **2015**, *14*, 826−832.

(8) Liang, L. B.; Wang, J.; Lin, W. Z.; Sumpter, B. G.; Meunier, V.; Pan, M. H. *Nano Lett.* **2014**, *14*, 6400−6406.

(9) Li, Y. F.; Zhou, Z.; Zhang, S. B.; Chen, Z. F. *J. Am. Chem. Soc.* **2008**, *130*, 16739−16744.

(10) Lee, G. H.; Cui, X.; Kim, Y. D.; Arefe, G.; Zhang, X.; Lee, C. H.; Ye, F.; Watanabe, K.; Taniguchi, T.; Kim, P.; Hone, J. *ACS Nano* **2015**, *9*, 7019−7026.

(11) Rong, Y. M.; He, K.; Pacios, M.; Robertson, A. W.; Bhaskaran, H.; Warner, J. H. *ACS Nano* **2015**, *9*, 3695−3703.

(12) Ly, T. H.; Chiu, M. H.; Li, M. Y.; Zhao, J.; Perello, D. J.; Cichocka, M. O.; Oh, H. M.; Chae, S. H.; Jeong, H. Y.; Yao, F.; Li, L. J.; Lee, Y. H. *ACS Nano* **2014**, *8*, 11401−11408.

(13) Zhang, Y.; Zhang, Y. F.; Ji, Q. Q.; Ju, J.; Yuan, H. T.; Shi, J. P.; Gao, T.; Ma, D. L.; Liu, M. X.; Chen, Y. B.; Song, X. J.; Hwang, H. Y.; Cui, Y.; Liu, Z. F. *ACS Nano* **2013**, *7*, 8963−8971.

(14) Gao, J.; Chow, P.; Thomas, A.; Lu, T.; Borca-Tasciuc, T.; Koratkar, N. *Appl. Phys. Lett.* **2014**, *105*, 123108.

(15) Kim, K. K.; Hsu, A.; Jia, X. T.; Kim, S. M.; Shi, Y. S.; Hofmann, M.; Nezich, D.; Rodriguez-Nieva, J. F.; Dresselhaus, M.; Palacios, T.; Kong, J. *Nano Lett.* **2012**, *12*, 161−166.

(16) Wood, J. D.; Wells, S. A.; Jariwala, D.; Chen, K. S.; Cho, E.; Sangwan, V. K.; Liu, X. L.; Lauhon, L. J.; Marks, T. J.; Hersam, M. C. *Nano Lett.* **2014**, *14*, 6964−6970.

(17) Chow, P. K.; Singh, E.; Viana, B. C.; Gao, J.; Luo, J.; Li, J.; Lin, Z.; Elias, A. L.; Shi, Y. F.; Wang, Z. K.; Terrones, M.; Koratkar, N. *ACS Nano* **2015**, *9*, 3023−3031.

(18) Mouri, S.; Miyauchi, Y.; Matsuda, K. *Nano Lett.* **2013**, *13*, 5944−5948.

(19) Tongay, S.; Sahin, H.; Ko, C.; Luce, A.; Fan, W.; Liu, K.; Zhou, J.; Huang, Y. S.; Ho, C. H.; Yan, J. Y.; Ogletree, D. F.; Aloni, S.; Ji, J.; Li, S. S.; Li, J. B.; Peeters, F. M.; Wu, J. Q. *Nat. Commun.* **2014**, *5*, 3252.

(20) Splendiani, A.; Sun, L.; Zhang, Y. B.; Li, T. S.; Kim, J.; Chim, C. Y.; Galli, G.; Wang, F. *Nano Lett.* **2010**, *10*, 1271−1275.

(21) Keyshar, K.; Gong, Y. J.; Ye, G. L.; Brunetto, G.; Zhou, W.; Cole, D. P.; Hackenberg, K.; He, Y. M.; Machado, L.; Kabbani, M.; Hart, A. H. C.; Li, B.; Galvao, D. S.; George, A.; Vajtai, R.; Tiwary, C. S.; Ajayan, P. M. *Adv. Mater.* **2015**, *27*, 4640−4648.

(22) He, X. X.; Liu, F. C.; Hu, P.; Fu, W.; Wang, X. L.; Zeng, Q. S.; Zhao, W.; Liu, Z. *Small* **2015**, *11*, 5423−5429.

(23) Zhang, E.; Jin, Y. B.; Yuan, X.; Wang, W. Y.; Zhang, C.; Tang, L.; Liu, S. S.; Zhou, P.; Hu, W. D.; Xiu, F. X. *Adv. Funct. Mater.* **2015**, *25*, 4076−4082.

(24) Zhang, Q.; Tan, S.; Mendes, R. G.; Sun, Z.; Chen, Y.; Kong, X.; Xue, Y.; Rümmeli, M. H.; Wu, X.; Chen, S.; Fu, L. *Adv. Mater.* **2016**, *28*, 2616−2623.

(25) Feng, Y. Q.; Zhou, W.; Wang, Y. J.; Zhou, J.; Liu, E. F.; Fu, Y. J.; Ni, Z. H.; Wu, X. L.; Yuan, H. T.; Miao, F.; Wang, B. G.; Wan, X. G.; Xing, D. Y. *Phys. Rev. B: Condens. Matter Mater. Phys.* **2015**, *92*, 054110.

(26) Chenet, D. A.; Aslan, O. B.; Huang, P. Y.; Fan, C.; van der Zande, A. M.; Heinz, T. F.; Hone, J. C. *Nano Lett.* **2015**, *15*, 5667−5672.

(27) Fujita, T.; Ito, Y.; Tan, Y. W.; Yamaguchi, H.; Hojo, D.; Hirata, A.; Voiry, D.; Chhowalla, M.; Chen, M. W. *Nanoscale* **2014**, *6*, 12458−12462.

(28) Bruce, P. G.; Freunberger, S. A.; Hardwick, L. J.; Tarascon, J.-M. *Nat. Mater.* **2012**, *11*, 19−29.

(29) Yin, Y. X.; Xin, S.; Guo, Y. G.; Wan, L. J. *Angew. Chem., Int. Ed.* **2013**, *52*, 13186−13200.

(30) Zhang, Q. F.; Wang, Y. P.; Seh, Z. W.; Fu, Z. H.; Zhang, R. F.; Cui, Y. *Nano Lett.* **2015**, *15*, 3780−3786.

(31) Manthiram, A.; Fu, Y. Z.; Su, Y. S. *Acc. Chem. Res.* **2013**, *46*, 1125−1134.

(32) Yuan, Z.; Peng, H. J.; Hou, T. Z.; Huang, J. Q.; Chen, C. M.; Wang, D. W.; Cheng, X. B.; Wei, F.; Zhang, Q. *Nano Lett.* **2016**, *16*, 519−527.

(33) Qiu, Y. C.; Li, W. F.; Zhao, W.; Li, G. Z.; Hou, Y.; Liu, M. N.; Zhou, L. S.; Ye, F. M.; Li, H. F.; Wei, Z. H.; Yang, S. H.; Duan, W. H.; Ye, Y. F.; Guo, J. H.; Zhang, Y. G. *Nano Lett.* **2014**, *14*, 4821−4827.

(34) Zhou, G. M.; Yin, L. C.; Wang, D. W.; Li, L.; Pei, S. F.; Gentle, I. R.; Li, F.; Cheng, H. M. *ACS Nano* **2013**, *7*, 5367−5375.

(35) Maillard, F.; Bonnefont, A.; Chatenet, M.; Guetaz, L.; Doisneau-Cottignies, B.; Roussel, H.; Stimming, U. *Electrochim. Acta* **2007**, *53*, 811−822.

(36) Li, Y. G.; Wang, H. L.; Xie, L. M.; Liang, Y. Y.; Hong, G. S.; Dai, H. J. *J. Am. Chem. Soc.* **2011**, *133*, 7296−7299.

(37) Ding, Q.; Meng, F.; English, C. R.; Caban-Acevedo, M.; Shearer, M. J.; Liang, D.; Daniel, A. S.; Hamers, R. J.; Jin, S. *J. Am. Chem. Soc.* **2014**, *136*, 8504−8507.

(38) Xiang, Q. J.; Yu, J. G.; Jaroniec, M. *J. Am. Chem. Soc.* **2012**, *134*, 6575−6578.

(39) Ye, G. L.; Gong, Y. J.; Lin, J. H.; Li, B.; He, Y. M.; Pantelides, S. T.; Zhou, W.; Vajtai, R.; Ajayan, P. M. *Nano Lett.* **2016**, *16*, 1097−1103.

(40) Voiry, D.; Yamaguchi, H.; Li, J. W.; Silva, R.; Alves, D. C. B.; Fujita, T.; Chen, M. W.; Asefa, T.; Shenoy, V. B.; Eda, G.; Chhowalla, M. *Nat. Mater.* **2013**, *12*, 850−855.

(41) Li, H.; Tsai, C.; Koh, A. L.; Cai, L. L.; Contryman, A. W.; Fragapane, A. H.; Zhao, J. H.; Han, H. S.; Manoharan, H. C.; Abild-Pedersen, F.; Norskov, J. K.; Zheng, X. L. *Nat. Mater.* **2015**, *15*, 48−53.

(42) Hinnemann, B.; Moses, P. G.; Bonde, J.; Jorgensen, K. P.; Nielsen, J. H.; Horch, S.; Chorkendorff, I.; Norskov, J. K. *J. Am. Chem. Soc.* **2005**, *127*, 5308−5309.

(43) Jaramillo, T. F.; Jorgensen, K. P.; Bonde, J.; Nielsen, J. H.; Horch, S.; Chorkendorff, I. *Science* **2007**, *317*, 100−102.

(44) Xiong, F.; Wang, H. T.; Liu, X. G.; Sun, J.; Brongersma, M.; Pop, E.; Cui, Y. *Nano Lett.* **2015**, *15*, 6777−6784.

(45) Wang, H. T.; Zhang, Q. F.; Yao, H. B.; Liang, Z.; Lee, H. W.; Hsu, P. C.; Zheng, G. Y.; Cui, Y. *Nano Lett.* **2014**, *14*, 7138−7144.

(46) Shi, J. P.; Ma, D. L.; Han, G. F.; Zhang, Y.; Ji, Q. Q.; Gao, T.; Sun, J. Y.; Song, X. J.; Li, C.; Zhang, Y. S.; Lang, X. Y.; Zhang, Y. F.; Liu, Z. F. *ACS Nano* **2014**, *8*, 10196−10204.